The following resources related to this article are available online at
www.sciencemag.org (this information is current as of January 15, 2009):

Updated information and services, including high-resolution figures, can be found in the online version of this article at:
http://www.sciencemag.org/cgi/content/full/323/5912/362

Supporting Online Material can be found at:
http://www.sciencemag.org/cgi/content/full/323/5912/362/DC1

This article **cites 23 articles**, 4 of which can be accessed for free:
http://www.sciencemag.org/cgi/content/full/323/5912/362#otherarticles

This article appears in the following **subject collections**:
Materials Science
http://www.sciencemag.org/cgi/collection/mat_sci

Information about obtaining **reprints** of this article or about obtaining **permission to reproduce this article** in whole or in part can be found at:
http://www.sciencemag.org/about/permissions.dtl

References and Notes

1. F. J. Millero, *Chemical Oceanography* (CRC Press, Boca Raton, FL, ed. 3, 2006).
2. R. A. Feely *et al.*, *Science* **305**, 362 (2004).
3. R. Schiebel, *Global Biogeochem. Cycles* **16**, 1065 (2002).
4. J. D. Milliman, A. W. Droxler, *Geol. Rundsch.* **85**, 496 (1996).
5. K. Lee, *Limnol. Oceanogr.* **46**, 1287 (2001).
6. D. Iglesias-Rodriguez *et al.*, *Eos Trans. AGU* **83**, 365 (2002).
7. J. D. Milliman *et al.*, *Deep Sea Res. Part I Oceanogr. Res. Pap.* **46**, 1653 (1999).
8. P. J. Walsh, P. Blackwelder, K. A. Gill, E. Danulat, T. P. Mommsen, *Limnol. Oceanogr.* **36**, 1227 (1991).
9. R. W. Wilson, K. M. Gilmour, R. P. Henry, C. M. Wood, *J. Exp. Biol.* **199**, 2331 (1996).
10. R. W. Wilson, J. M. Wilson, M. Grosell, *Biochim. Biophys. Acta* **1566**, 182 (2002).
11. M. Grosell, *J. Exp. Biol.* **209**, 2813 (2006).
12. R. W. Wilson, M. Grosell, *Biochim. Biophys. Acta* **1618**, 163 (2003).
13. J. Genz, J. R. Taylor, M. Grosell, *J. Exp. Biol.* **211**, 2327 (2008).
14. A. Clarke, N. M. Johnstone, *J. Anim. Ecol.* **68**, 893 (1999).
15. S. Jennings *et al.*, *Proc. R. Soc. London B. Biol. Sci.* **275**, 1375 10.1098/rspb.2008.0192 (2008).
16. V. Christensen *et al.*, *Models of the World's Large Marine Ecosystems. GEF/LME Global Project Promoting Ecosystem-Based Approaches to Fisheries Conservation and Large Marine Ecosystems* (IOC Technical Series No. **80**, UNESCO, 2008).
17. W. S. Broecker, in *The Fate of Fossil CO₂ in the Oceans*, N. R. Anderson, A. Malahoff, Eds. (Plenum, New York, 1977), p. 207.
18. R. A. Feely *et al.*, *Global Biogeochem. Cycles* **16**, 1144 (2002).
19. C. L. Sabine, R. M. Key, R. A. Feely, D. Greeley, *Global Biogeochem. Cycles* **16**, 1067 (2002).
20. S. Chung *et al.*, *Global Biogeochem. Cycles* **17**, 1093 (2003).
21. C. L. Sabine *et al.*, in *The Global Carbon Cycle: Integrating Humans, Climate, and the Natural World*, C. B. Field, M. R. Raupach, Eds. (Island Press, Washington, DC, 2004), pp. 17–44.
22. T. Takahashi, *Spec. Publ. Cushman Found. Foraminiferal Res.* **13**, 11 (1975).
23. J. K. B. Bishop, J. C. Stepien, P. H. Wiebe, *Prog. Oceanogr.* **17**, 1 (1986).
24. R. P. Harris, *Mar. Biol. (Berlin)* **119**, 431 (1994).
25. P. Van der Wal, R. S. Kempers, M. J. W. Veldhuis, *Mar. Ecol. Prog. Ser.* **126**, 247 (1995).
26. D. W. Pond, R. P. Harris, C. A. Brownlee, *Mar. Biol. (Berlin)* **123**, 75 (1995).
27. H. Jansen, D. A. Wolf-Gladrow, *Mar. Ecol. Prog. Ser.* **221**, 199 (2001).
28. R. H. Byrne, J. G. Acker, P. R. Betzer, R. A. Feely, M. H. Cates, *Nature* **312**, 321 (1984).
29. R. A. Feely *et al.*, *Mar. Chem.* **25**, 227 (1988).
30. J. W. Morse, F. T. Mackenzie, *Geochemistry of Sedimentary Carbonates* (Elsevier, New York, 1990).
31. J. W. Morse, D. K. Gledhill, F. J. Millero, *Geochim. Cosmochim. Acta* **67**, 2819 (2003).
32. V. J. Fabry, W. G. Deuser, *Deep-Sea Res.* **38**, 713 (1991).
33. J. C. Orr *et al.*, *Nature* **437**, 681 (2005).
34. H. O. Pörtner, M. Langenbuch, A. Reipschläger, *J. Oceanogr.* **60**, 705 (2004).
35. B. A. Seibel, P. J. Walsh, *Science* **294**, 319 (2001).
36. M. Grosell *et al.*, *Am. J. Physiol. Regul. Integr. Comp. Physiol.* **288**, R936 (2005).
37. V. J. Fabry, *Science* **320**, 1020 (2008).
38. R.W.W. acknowledges support from the UK Biotechnology and Biological Sciences Research Council (awards BB/D005108/1, BB/F009364/1, and ISIS 1766) and The Royal Society (award RSRG 24241). F.J.M. acknowledges the Oceanographic Section of the U.S. National Science Foundation (NSF). P.J.W. is supported by the Natural Sciences and Engineering Research Council (NSERC) of Canada and the Canada Research Chair program. V.C. acknowledges support from NSERC, the Global Environment Facility's UNEP/UNESCO/IOC (Intergovernmental Oceanographic Commission) LME (Large Marine Ecosystem) activities, and from the Sea Around Us Project, initiated and funded by The Pew Charitable Trusts. S.J. thanks the European Commission and the UK Department of Environment, Food, and Rural Affairs for funding support, and A. Clarke (British Antarctic Survey, Cambridge) for providing a compilation of fish oxygen consumption data. M.G. and S.J. are supported by the NSF (awards 0416440, 0714024, and 0743903). We also thank referees for their insightful comments; K. Knapp (School of Physics, University of Exeter) for the fish x-ray images (Fig. 2); R. Walton (University of Warwick, UK) for the powder x-ray diffraction analysis (fig. S1); H. Stoll (Department of Geoscience, Williams College, Williamstown, MA) and A. Pritchard (University of Exeter, Biosciences) for the scanning electron micrographs of sediment trap samples and fish carbonates, respectively (fig. S3); R. Forster (Centre for Environment, Fisheries and Aquaculture Science, Lowestoft) for plotting fig. S4; FishBase (www.fishbase.org) for providing fish species' information; J. Whittamore for preparation of flounder for x-ray imaging; J. Corcoran and C. Cooper for the sheepshead minnow experiments in the Supporting Online Material; and R. van Aerle for assistance with graphical illustrations.

Morphogenesis of Self-Assembled Nanocrystalline Materials of Barium Carbonate and Silica

Juan Manuel García-Ruiz,[1] Emilio Melero-García,[1] Stephen T. Hyde[2]

The precipitation of barium or strontium carbonates in alkaline silica-rich environments leads to crystalline aggregates that have been named silica/carbonate biomorphs because their morphology resembles that of primitive organisms. These aggregates are self-assembled materials of purely inorganic origin, with an amorphous phase of silica intimately intertwined with a carbonate nanocrystalline phase. We propose a mechanism that explains all the morphologies described for biomorphs. Chemically coupled coprecipitation of carbonate and silica leads to fibrillation of the growing front and to laminar structures that experience curling at their growing rim. These curls propagate in a surflike way along the rim of the laminae. We show that all observed morphologies with smoothly varying positive or negative Gaussian curvatures can be explained by the combined growth of counterpropagating curls and growing laminae.

The theoretical morphology of classical crystals is well accommodated within conventional crystal growth theory, where the development of various crystal faces is accounted for by the relative crystallographic surface energies at the atomic scale, and the overall symmetry is imposed by the atomic-scale packing. The relation between nonequilibrium crystal shapes and their physical and chemical growth conditions is also part of the general picture (*1*). In contrast, despite numerous observations over the years (*2*) that life is able to make precise, smooth, differentiable shapes made of polycrystalline minerals (shells, teeth, bones, etc.), we have a limited understanding of the morphogenetical mechanisms leading to the formation of these fascinating architectures. The laboratory synthesis of actual self-assembled structures mimicking the ability of life to create sinuous noncrystallographic morphologies with crystalline materials is still a challenge. Among the few examples of synthetic self-organized nanocrystalline materials known to display a wealth of morphologies comparable to that of biominerals are silica/carbonate biomorphs (*3–5*). Biomorphs, like biominerals, exhibit nanoscale atomic ordering but lack long-range positional order. As a consequence, no characteristic faces or edges are expressed; rather, they are bounded by smoothly curved surfaces. Thus biomorphs, whose morphogenetic mechanism has remained unknown (*5–7*), display a zoo of curvilinear morphologies, often indistinguishable from the forms of biomaterials found in vivo.

Silica/barium carbonate biomorphs can be grown routinely by mixing barium chloride solutions with silica solutions and gels within a pH range from 8.5 to 11, at atmospheric pressure and temperature (*8*). Under alkaline conditions, carbonate from dissolved atmospheric CO_2 reacts with Ba^{2+} to precipitate crystalline barium carbonate (witherite) in the form of pseudohexagonal prismatic crystals tapered by bipyramidal faces (*9*). However, it has been shown (*3–7*, *10*, *11*) that when barium carbonate crystallizes from silica-rich solutions or from silica gels, it forms polycrystalline aggregates displaying a variety of

[1]Laboratorio de Estudios Cristalográficos, Instituto Andaluz de Ciencias de la Tierra, Consejo Superior de Investígaciones Científicas–Universidad de Granada, Avenida del Conocimiento, Parque Tecnológico, Ciencias de la Salud, 18100 Armilla, Spain. [2]Department of Applied Mathematics, Research School of Physical Sciences, Australian National University, Canberra, Australian Capital Territory 0200, Australia.

micrometer- to millimeter-sized morphologies with noncrystallographic symmetry shaped by "differentiable" surfaces of well-defined and smoothly varying Gaussian curvature. Its sub-micrometer structure has been shown to be composed of nanometer-sized rods of witherite, whose mutual arrangement is characterized by a high degree of orientational order but no translational order. The carbonate nanocrystals are coated by amorphous silica (SiO_2) that also cements the structure, thus forming a composite material, as demonstrated by the ability to selectively dissolve the crystalline or amorphous phase with either dilute HCl or NaOH solutions, respectively (12).

We used time-lapse video microscopy and electron microscopy to monitor the formation, growth development, and final morphology and textures of witherite biomorphs (8). Our observations have established that the core of all these morphologies is a pseudohexagonal twinned prismatic crystal of witherite that grows preferentially along the c axis (Fig. 1A). The morphologies seem
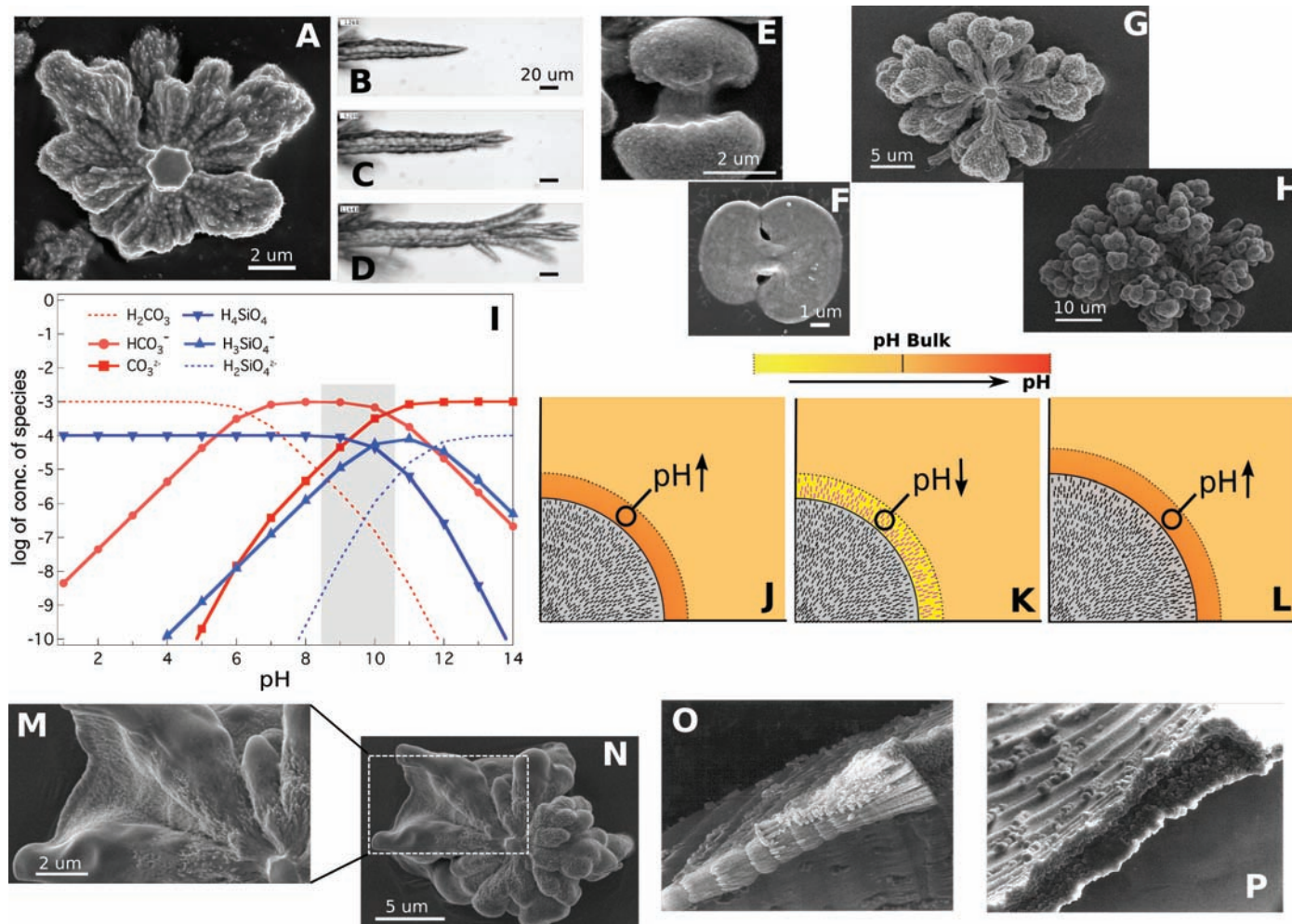
to arise from the breaking of the crystallographic symmetry of this crystal core of carbonate that occurs along two consecutive but different routes. The first of these routes goes from crystallographic symmetry toward dilation symmetry, whereas the second continues toward rotational symmetry. The dilation route ends in fractal cauliflowerlike morphologies, whereas the rotational route ends in three-dimensional (3D) microstructures displaying a wealth of smoothly curved surfaces of uniformly varying Gaussian curvature.

The crystallographic symmetry is initially broken toward dilation symmetry by the splitting of the basal pinacoid {001} or the pseudohexagonal bipyramidal faces of the growing crystal core. Because of pioneering work by Keith and Paden (13), crystal splitting at noncrystallographic angles can be explained by the concentration at the growth front of nonabsorbable polymeric impurities, which are pushed ahead of the growing crystal and cause the formation of 2D islands that are slightly misoriented with respect to the crystalline lattice (13–15). These islands continue to

grow, forming a tilted outgrowth displaying a noncrystallographic angle with the initial seed (Fig. 1, B to D). Under alkaline conditions, as a result of the chemical coupling between the precipitation of carbonate and silica, the precipitation process of the crystalline carbonate phase triggers the formation of polymeric impurities at the crystallization front, which in turn triggers the precipitation of carbonate. This chemical feedback process occurs as follows: During the crystallization of barium carbonate, there is a continuous removal of carbonate groups, which decreases the pH of the local environment surrounding the growing crystals according to the reactions $Ba^{2+} + CO_3^{2-} \leftrightarrows BaCO_3$ and $HCO_3^- + H_2O \leftrightarrows H_3O^+ + CO_3^{2-}$.

On the other hand, the precipitation of amorphous silica occurs exclusively by the condensation of molecules of silicic acid $Si(OH)_4$ (16). At alkaline pH, the silicic acid deprotonates according to $Si(OH)_4 \leftrightarrows SiO(OH)_3^- + H_3O^+$ at pH = 9 and $SiO(OH)_3^- \leftrightarrows SiO_2(OH)_2^{2-} + H_3O^+$ at pH = 10.7.

Therefore, the decrease of pH caused by the precipitation of carbonate increases the local super-

Fig. 1. The breaking of the crystallographic symmetry and chemical coupling. (**A** to **H**) illustrate the transition from a single pseudohexagonal crystal core shown in (A) to sheaf-of-wheat [(E) and (F)] and globular [(G) and (H)] structures, through splitting of the pinacoidal or bypyramidal tip of the crystal core [(B) to (D)]. [(B) to (D)] are frames of a video (movie S4). (**I**) shows the concentration of the chemical species as a function of pH (29) and the pH region (gray) at which these structures form. (**J** to **L**) show schematically the growing of the fibrillated front due to the local oscillations of pH driven by the coupled precipitation of silica and carbonate. The last four panels show the beginning of the formation (**M** and **N**) and details of the laminar structures (**O** and **P**).

saturation of silicic acid in the vicinity of the growing carbonate crystals, thus provoking the adsorption and precipitation of silica on their positively charged surfaces (*17*), poisoning crystal growth and causing bifurcation of the crystals. This chemical coupling ensures continuous splitting at noncrystallographic angles, leading to the formation of sheaf-of-wheat structures and, on further growth, to space-filling cauliflowerlike structures (Fig. 1, E to H) (*18*, *19*).

At elevated pH values, typical of biomorph growth conditions, the silica solubility is more sensitive to changes in pH value (Fig. 1I). Therefore, the amount of silica coating the nanocrystals is large enough to provoke the cessation of carbonate crystal growth. In turn, the precipitation of amorphous silica increases the local pH by converting the acidic –OH groups into siloxane bonds. This increase in pH promotes the formation of additional carbonate ions, increasing the barium carbonate supersaturation and leading to a further round of carbonate nucleation in the form of 3D nuclei (Fig. 1, J to L). This process causes the single-crystal growth front to fragment, creating a polycrystalline front of nanocrystals co-oriented with the single crystal. We call this transformation fibrillation. Despite the fibrillation mechanism being due to the oscillatory behavior of pH at the growth front, this does not necessarily yield oscillatory dynamics of the growth front.

Subsequent silica precipitation prevents these nuclei from growing larger than the size of a few tens to hundreds of nanometers before they become almost fully coated with silica, therefore bearing an overall negative charge at alkaline pH. Mutual repulsion between these witherite-silica particles is screened by the cations (Na^+ and excess Ba^{2+}) in solution. As a consequence, the nanocrystals of witherite-silica experience only weak interaction forces that must be attractive to account for the observed near co-orientation of the particles along their long axis. Co-orientation can be stabilized by the condensation of silanol groups and the formation of siloxane bonds between neighbor witherite-silica particles (*16*). However, the absence of strict translational order between the nanocrystals is also suggestive of a weak interparticle interaction.

Eventually, via fibrillation, a transition from continuously splitting crystals to laminar nanocrystalline aggregates with macroscopic radial symmetry occurs (Fig. 1, M to P). The final voluptuous morphologies characteristic of biomorphs grow in the absence of crystallographic constraints by the following mechanism. The growth front of the lamina advances linearly with time, and because the radial growth rate is independent of the azimuthal angle φ, the lamina initially forms a circular disc with an arced growth edge. Time-lapse microscopy reveals the forma-

tion of a small curled lip at some single point of the growth edge. The curling induces the following at this single point: (i) the cessation of growth along the radial direction, and (ii) the formation of two new growth fronts located on the right and left of the curl (movie S1). The growth fronts propagate the curling along the perimeter of the lamina, much as a surfing wave forms a quasi-tubular rim (Fig. 2A). As the curling advances along the rim of the circular lamina, it arrests the radial propagation of the structure: The curling front propagates at constant velocity tangentially to the circular perimeter, while the radial velocity of the curled perimeter becomes zero. As a result, the point at which the flat lamina starts to curl follows a trajectory that is the result of orthogonal growth fronts: the radial growth velocity V_ρ of the lamina and the azimuthal velocity of propagation V_φ of the curl as shown in Fig. 2B. When two curling fronts approach each other along the rim from opposite directions (irrespective of whether they arise from the same or different curling points) they describe the characteristic cardioid or leaflike shape of biomorphs because of the continuous reorientation of the growth edge induced by the accumulation of angles β', β'', and β''', whose origin is thus explained (Fig. 2, B to F).

This simple curl triggers a morphogenetic mechanism that explains the whole variety of 3D morphologies displayed by silica biomorphs. The parameters involved in the morphogenesis are the following (Fig. 2A): (i) The relative directionality of the curling, either right- (D) or left- (L) handed; (ii) the relative values of the azimuthal velocities V_φ of the two approaching curled rims, as well as those relative to the radial velocity V_ρ of the uncurled sheet; and (iii) the relative height H of the two approaching curls. The following characteristic biomorph forms emerge as specific cases of this mechanism.

1) Morphogenesis of leaflike shapes (L_1D_2 or D_1L_2; $H_1 = H_2$; $V_{\varphi 1}$ $V_{\varphi 2}$ V_ρ). To form a regular leaf, the two approaching curling fronts must bend with different handedness and their curling height must be of the same size. Thus, when the two curling rims meet, their growth fronts seal in a single cusp. The overall contour of the leaflike shape and the existence of a bilateral symmetry (a mirror plane across the cusp) depend on the relative rates of azimuthal growth (Fig. 2).
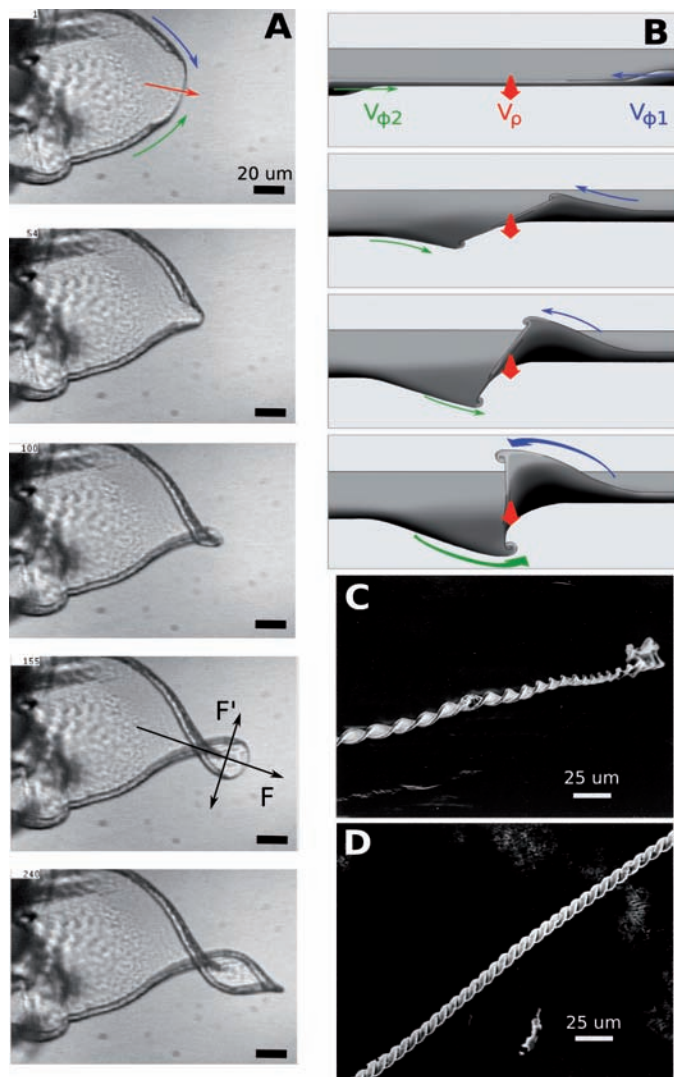
2) Morphogenesis of helicoids of constant width (L_1L_2 or D_1D_2; $H_1 = H_2$; $V_{\varphi 1} \approx V_{\varphi 2} \approx V_\rho$). The two approaching curled rims have the same handedness and similar heights. In addition, the azimuthal growth rates of both rims are similar and are similar to the rate of growth of the uncurled sheet. A perfect helicoid is formed, which advances linearly with time (Fig. 3).

3) Morphogenesis of helicoids of decreasing width (L_1L_2 or D_1D_2; $H_1 \approx H_2$; $V_{\varphi 1} \approx V_{\varphi 2} > V_\rho$). The two approaching curled rims have the same handedness and similar heights, but the azimuthal velocity of the rims is faster than the rate of growth of the uncurled sheet. The resulting
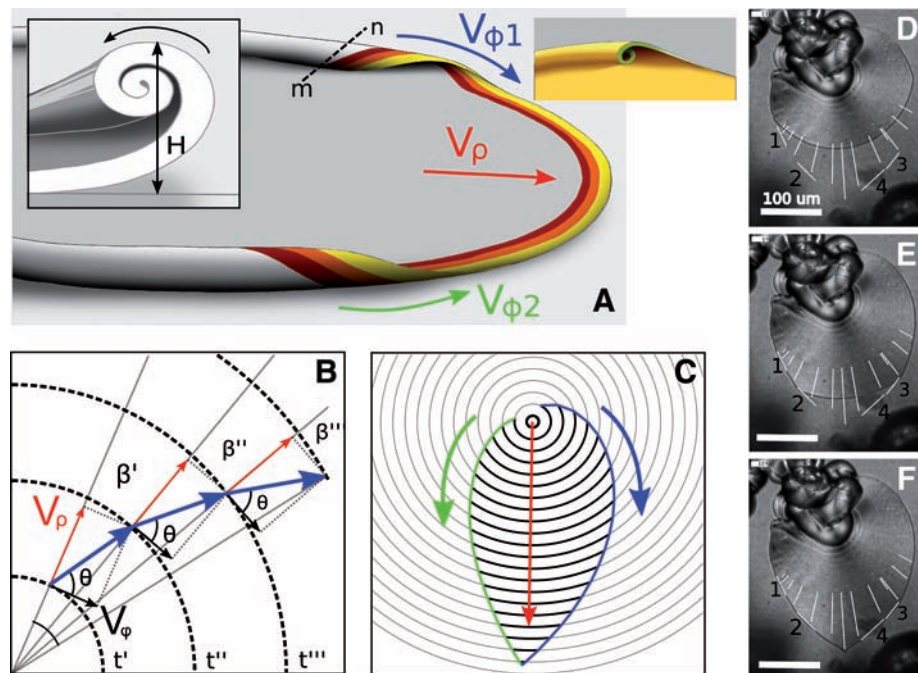
Fig. 2. Morphogenesis of the leaf and curl parameters described in the text. (**A**) shows an artist's view of two opposite-handed curls counterpropagating along the rim of a growing lamina. The inset shows a cross section of the curl (dashed line m-n) with the parameter H described in the text. The colors indicate the time history of the growth of the aggregate, and the yellow rim shows the current growth front. (**B** and **C**) show a scheme of the origin of the leaflike morphology as a result of the propagation of the curled front along the rim. The actual shape is determined by the ratio of the velocities $V_{\varphi 1}$, $V_{\varphi 2}$ of each moving curl and V_ρ that fixes the angle θ, and the specific point in space and time at which the curls originated. This is illustrated by frames D to F of movie S7, where the velocities were measured to be V_ρ= 0.91(3) µm/min along the radial white paths, and $V_{\varphi 2}$ = 2.0(3) µm/min (paths labeled 1 and 2) and $V_{\varphi 1}$ = 2.8(3) µm/min (paths labeled 3 and 4).

Fig. 3. Formation of helicoids. When two counter-propagating curls with the same handedness approach each other, the flat lamina continues to grow outward with velocity V_ρ. As the curls approach each other, the lamina bends, following the sense of the curls. (**A**) displays a series of frames of movie S8, showing the formation of a helicoid. (**B**) is a front-view illustration of two like-handed curls twisting to produce a helix. Different types of helicoidal morphologies are produced, depending on the relative growth rates. For equal or nearly equal azimuthal velocities of the two curled fronts, comparable with the radial growth rate V_ρ, the lamina and the two curled rims are locked into a coupled growth process, in which the curls propagate along the rims of a central lamina, leading to continuous twisting with the sense along the direction F indicated in (A). Because the growth of the central lamina in the direction F' perpendicular to F is hindered by the propagation of the curlings along its rim, a helicoid of approximately constant width sprouts from the site of the lamina where the approaching curls meet. (**C** and **D**) show scanning electron microscopy views of a helicoid with constant width and of a braid, respectively.

helicoids display constant pitch but have linearly decreasing diameter. If $V_{\varphi 1}$ and $V_{\varphi 2}$, are different but still larger than V_ρ, the diameter of the helicoids decreases asymmetrically (movie S2).

4) Morphogenesis of braids ($L_1 L_2$ or $D_1 D_2$; $H_1 \approx H_2$; $V_{\varphi 1} \approx V_{\varphi 2} > V_\rho$). The azimuthal growth rates of the two rims are much faster than the radial velocity of the uncurled lamina. Therefore, the uncurled lamina is overtaken by a braid that forms because the two curls of the same handedness coil onto each other (Fig. 3D).

5) Morphogenesis of wormlike structures ($L_1 L_2$ or $D_1 D_2$ or $L_1 D_2$; $H_1 \gg H_2$; $V_{\varphi 1}$; $V_{\varphi 2}$; V_ρ). If the height and azimuthal growth rate of one of the curls is much larger than the other, regardless of the handedness of the rims, upon interaction it ends up coiling on itself. That infolding can grow forward or backward, yielding the wormlike morphologies displayed by some silica biomorphs (movies S3 to S5).

It is worth noticing that all the twisted shapes result when the two curls have the same hand-edness. Because either enantiomorph has an equal probability of forming, no chiral bias can be expected, and silica biomorphs are by nature racemic.

The proposed growth mechanism explains a number of symmetry properties of silica biomorphs that have remained a puzzle for several years. The leaf shape, so characteristic of silica biomorphs, is an inevitable result of the opposing and mutually interacting surfing curls. Further, regular forms, with uniform curvature distributions over their surface (such as twisted spheres and generic twisted surfaces), are less common than irregular shapes because geometric regularity in this sense requires fixed ratios of growth rates over extended times. This mechanism also explains the absence of chirality in silica biomorphs, because the handedness of the helical structures depends on the relative sign of curl, which is arbitrary. Finally, this mechanism explains the failure to induce chirality in silica biomorphs with the use of chiral molecules: The origin of the curling is at a much larger length scale and is therefore uncoupled from molecular chemistry.

The combined curling and radial growth phenomenology outlined here produces the variety of curvilinear forms observed in biomorphs, without the presence of biomolecular agents, such as proteins, to steer growth via surface adsorption. It follows that complex curved shapes are not exclusive to biology. This morphogenetical mechanism may contribute to the morphogenesis of other exotic inorganic precipitates (20–23). It also shows that evidence for nanobacteria (24) and ancient terrestrial (3, 25) and Martian (26–28) life remnants cannot rest on morphology alone.

References and Notes
1. I. Sunagawa, *Crystals: Growth, Morphology and Perfection* (Cambridge Univ. Press, Cambridge, 2005).
2. D. W. Thompson, *On Growth and Form* (Cambridge Univ. Press, Cambridge, 1942).
3. J. M. García-Ruiz *et al.*, *Science* **302**, 1194 (2003).
4. J. M. García Ruiz, *Geology* **26**, 843 (1998).
5. S. T. Hyde, A. M. Carnerup, A. Larsson, A. G. Christy, J. M. García-Ruiz, *Physica A* **339**, 24 (2004).
6. T. Terada, S. Yamabi, H. Imai, *J. Cryst. Growth* **253**, 435 (2003).
7. J. M. García-Ruiz, *J. Cryst. Growth* **73**, 251 (1985).
8. Materials and methods are available as supporting material on *Science* Online.
9. F. Lippmann, *Sedimentary Carbonate Minerals* (Springer, Berlin, 1973).
10. E. Bittarello, D. Aquilano, *Eur. J. Mineral.* **19**, 345 (2007).
11. A. E. Voinescu *et al.*, *J. Cryst. Growth* **306**, 152 (2007).
12. J. M. Garcia-Ruiz, J. L. Amorós, *J. Cryst. Growth* **55**, 379 (1981).
13. H. D. Keith, F. J. Padden, *J. Appl. Phys.* **34**, 2409 (1963).
14. N. Goldenfeld, *J. Cryst. Growth* **84**, 601 (1987).
15. P. Philips, in *Handbook of Crystal Growth* (Elsevier, Amsterdam, 1993), vol. 2, chap. 18, pp. 1169–1216.
16. R. K. Iler, *The Chemistry of Silica* (Wiley, New York, 1979).
17. C.-C. Li, J.-H. Jean, *J. Am. Ceram. Soc.* **85**, 2977 (2002).
18. D. P. Grigoriev, *Ontogeny of Minerals* (Israel Program for Scientific Translation, Jerusalem, Israel, 1965).
19. M. N. Maleev, *Tschermaks Mineral. Petrogr. Mitt.* **18**, 1 (1972).
20. H. Cölfen, *Curr. Opin. Colloid Interface Sci.* **8**, 23 (2003).
21. H. Cölfen, M. Antonietti, *Angew. Chem. Int. Ed.* **44**, 5576 (2005).
22. L. B. Gower, D. J. Odom, *J. Cryst. Growth* **210**, 719 (2000).
23. S. Mann, G. A. Ozin, *Nature* **382**, 313 (1996).
24. J. Martel, D. J. Young, *Proc. Natl. Acad. Sci. U.S.A.* **105**, 5549 (2008).
25. J. M. García-Ruiz, A. Carnerup, A. G. Christy, N. J. Welham, S. T. Hyde, *Astrobiology* **2**, 353 (2002).
26. F. Poulet *et al.*, *Nature* **438**, 623 (2005).
27. J. F. Mustard *et al.*, *Nature* **454**, 305 (2008).
28. F. Westall, *Space Sci. Rev.* **135**, 95 (2008).
29. C. B. Andersen, *J. Geosci. Edu.* **50**, 389 (2002).
30. We are grateful to N. J. Welham (Australian National University, now at the University of Ballarat) for some of the videomicroscopy recordings. This work was supported by the Spanish Ministry of Education and Science (project MAT2006-11701) and is part of the Consolider-Ingenio 2010 project Factoría Española de Cristalización. E.M.-G. acknowledges financial support from the program Juan de la Cierva (Ministerio de Innovación y Ciencia). S.T.H. acknowledges the Australian Research Council for a Federation Fellowship.